Closing the loop: Lamellipodia dynamics from the perspective of front propagation

Yair Adler and Sefi Givli*

Faculty of Mechanical Engineering, Technion—Israel Institute of Technology, Haifa 32000, Israel

(Received 19 February 2013; revised manuscript received 25 July 2013; published 22 October 2013)

We develop a simple physical model that captures the large-scale lamellipodia dynamics in crawling cells and explains the observed spectrum of fish keratocytes behavior. The main ingredients in this description are the geometrical evolution of the lamellipodium leading edge, the dynamic remodeling of the actin network, and the interconnection between them. We deviate from existing theoretical works and consider the lamellipodium leading edge as a propagating front. The agreement of our model with experimental works suggests that the large-scale morphological and migration features exhibited by keratocyte cells are a direct consequence of the closed feedback loop between the shape of the leading edge and the density of the actin network.

DOI: 10.1103/PhysRevE.88.042708 PACS number(s): 87.10.Ed, 87.17.Aa

I. INTRODUCTION

An important class of cell motility is crawling over surfaces. Crawling cells move by three interrelated processes: actin protrusion at the cell front, retraction of the cell rear, and adhesion to the surface [1]. Crawling speed is highly variable for different cell types. For example, the fish epidermal keratocyte can move one cell diameter in about two minutes, as compared to about one hour required by the fibroblast. This stems from differences in the coordination between the aforementioned processes of protrusion, retraction, and anchorage [2]. Coordination is largely achieved by mechanical signals provided by the plasma membrane. In particular, membrane tension arises from the adhesion of the cytoskeleton and the membrane to the substrate as well as from forces generated by the motility machinery pushing the membrane from within the cell [3]. In turn, the membrane tension applies an opposing load that resists membrane extension and controls actin protrusion at the leading edge. Experimental measurements of migration features in a large number of live fish keratocyte cells revealed statistically significant correlations between various crawling features [4]. It was found that faster (slower) cells are generally more elongated (round), they have larger (smaller) radius of curvature, exhibit higher (lower) center-to-end actin density ratio, and their leading edge length is longer (shorter). In addition, it has been demonstrated by several groups that modifying the mechanical or chemical properties of the substrate has a dramatic effect on the keratocyte morphology, migration velocity, and stability. For example, Barnhart *et al.* [5] studied the effect of substrate adhesion strength. They found that cells migrating on a surface with intermediate adhesion strengths resembled stereotypical keratocytes, characterized by a broad lamellipodium and persistent shape. Cells at low adhesion strength were small and round with highly variable protrusion rates and nonpersistent shape, as illustrated in Fig. 1. Also, cells at high adhesion strength exhibited traveling waves of protrusion.

Our main goal is to develop a coarse grained description of the lamellipodium large scale dynamics that explains the observed spectrum of keratocyte behavior. The two main ingredients involved in this description are the shape of the leading edge and the actin concentration (number of actin filaments per unit length) along the leading edge. In this model, the tension in the plasma membrane manifests the interrelation with processes taking place at other regions of the cell, such as depolymerization, contraction, and adhesion. Thus the model provides a platform for studying how membrane tension affects the large-scale dynamics of the leading edge and in turn an understanding (though qualitative) of how adhesion, for example, affects the shape of the leading edge. This concept has been adopted before in, e.g., [4,6,7]. Yet these were limited to studying steady-state configurations or subjected to simplifying assumptions regarding the shape of the leading edge. Consequently, these models constitute a one-way interaction path between the shape of the leading edge and the distribution of the actin density along it. However, in reality, the shape of the leading edge affects the remodeling of the actin network and vice versa. This two-way coupling and its consequences are the main focus of this paper. We will show that the interconnection between shape and actin density forms a closed feedback loop that is responsible for the intriguing large-scale dynamics of lamellipodia in crawling cells. In order to account for these features we deviate from current modeling approaches of lamellipodia and formulate the evolution of the leading edge geometry from the perspective of front propagation. In the past three decades there has been growing interest in the mathematical description of front propagation as it applies to a wide range of phenomena in physical, chemical, and cross-disciplinary systems [8] such as population invasions, tumor growth, chemical waves, and crystallization [9–16]. By adopting this approach we are able to completely explain the aforementioned experimental observations regarding statistical correlations between motility features in keratocyte cells. In addition, we are able to study stability of steady-state configurations and find that crawling speed is limited by dynamic instability of the feedback loop rather than the maximum polymerization rate. This also explains the biphasic effect of cell-substrate adhesion on migration features [17–19]. We note that, in recent years, several models with varying degree of numerical complexity have been developed [20], including phase field models [21–23]. Our approach reduces significantly the complexity of the model, provides analytical insights, and directly builds on quantities with physical significance such as local curvature and membrane tension.

*givli@technion.ac.il

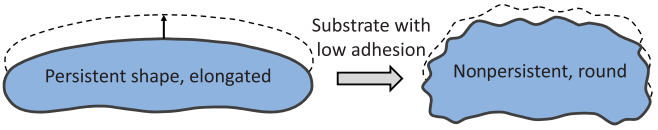

FIG. 1. (Color online) Experiments show that substrate properties significantly affect morphological features and dynamics behavior.

II. THEORETICAL MODEL

A schematic description of the model is shown in Fig. 2, which illustrates how the membrane shape and the actin concentration form a closed feedback loop. Below we detail the model assumptions and formulate the dynamic equations that govern the geometrical evolution of the leading edge shape and the evolution of the actin concentration along the leading edge.

A. Membrane tension and actin density dictate a graded normal velocity

Forces on the membrane at any point equilibrate within milliseconds [24] so that, on the time scales relevant for motility, membrane tension is spatially homogenous at all points along the cell boundary [25]. Thus, since the out-of-plane curvature of the membrane at the leading edge is much higher than the in-plane curvature, the Young-Laplace relation suggests that the membrane tension T imposes a spatially uniform opposing force (per unit length) on the actin network. The density of actin filaments along the leading edge is graded [4,6], thus the force per filament at location s along the leading edge is $f(s) = 2T/\rho(s)$. If the force per filament is small, the filaments are allowed to grow rapidly and advance the leading edge faster. In recent years, there has been a large effort to characterize this force-velocity relation both theoretically and experimentally, e.g., [26–28]. Although still debated, it is generally accepted that the relation between

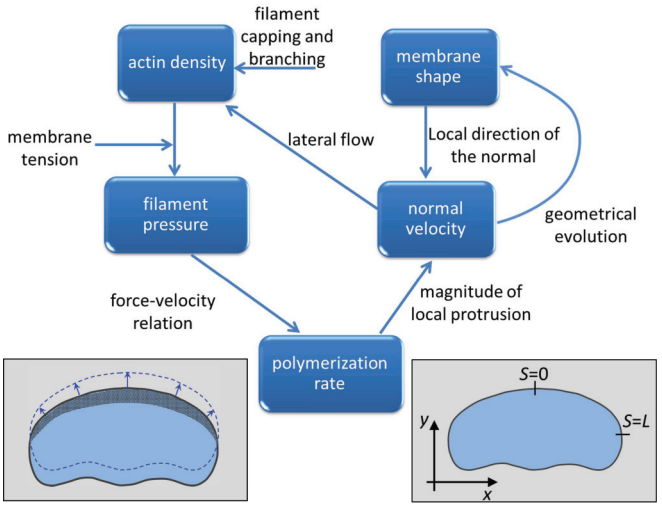

FIG. 2. (Color online) Schematic description of the model. The left inset shows the graded protrusion velocity (arrows) and actin density (gray shade) for a constant shape. A location on the leading edge can be expressed in terms of a laboratory coordinate system (x, y) or by the arclength s; see right inset.

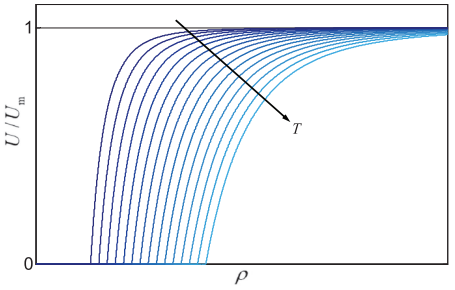

FIG. 3. (Color online) Membrane tension T affects the lamellipodia dynamics by altering the protrusion-density relation.

the force per filament and the protrusion rate of the actin network in the normal direction is characterized by a velocity that is insensitive to the load at low forces, whereas at high loads the velocity decreases with the load and vanishes at a characteristic stall force [28–30]. A simple mathematical form that fits the observed behavior is $U = U_m[1 - (f/f_{\text{stall}})^w]$. Here U_m is the maximal velocity, f_{stall} is the stall force, and w controls the concavity of the relation. Direct measurements in motile keratocytes suggest that $w \simeq 4$ for these cells [3,28]. We emphasize that our model is not limited to this specific mathematical form and that different forms will not have a significant influence on the results as long as they satisfy the aforementioned features of the force-velocity relation. Finally, by combining the force-velocity relation with the graded actin density, we conclude with a protrusion-density relation

$$\frac{U}{U_m} = 1 - \left(\frac{\rho_s}{\rho}\right)^w \quad \text{for} \quad \rho > \rho_s, \tag{1}$$

where $\rho_s = 2T/f_{\text{stall}}$ is the stall density below which the force per filament exceeds f_{stall}. Note that the stall density depends on the membrane tension. Thus, crawling on a substrate with different stiffness or adhesion strength, which affects the membrane tension [31,32], alters the protrusion-density relation, as illustrated in Fig. 3, and consequently changes the lamellipodia dynamics.

B. Geometrical evolution

The graded normal velocity $U(s)$ dictates the geometrical evolution (shape) of the lamellipodium leading edge. We mathematically describe the leading edge of the lamellipodium by a planar curve evolving dynamically in a two-dimensional space. This curve can be specified by the position vector $\vec{x}(\sigma, t)$, where t is time and σ is a spatial parameter. In particular, we choose σ such that it is preserved (constant in time) along the normal. It is convenient to express the dynamics of the curve in terms of gauge invariant geometrical quantities such as curvature κ and arclength s. These are related by the following standard relations:

$$s(\sigma) = \int_0^\sigma \sqrt{\frac{\partial \vec{x}}{\partial \sigma} \cdot \frac{\partial \vec{x}}{\partial \sigma}}\, d\sigma', \quad \hat{t} = \frac{\partial \vec{x}}{\partial s}, \quad \kappa = -\hat{n}\frac{\partial^2 \vec{x}}{\partial s^2}, \tag{2}$$

where $\hat{t}$ and $\hat{n}$ are the unit tangent and unit normal vectors, respectively. With the aid of standard tools from differential calculus and complex analysis, it can be shown that the

evolution of the curve shape $\kappa(s,t)$ is governed by the equation [33]

$$\frac{\partial \kappa}{\partial t} = -\left(\kappa^2 + \frac{\partial^2}{\partial s^2}\right)U - \frac{\partial \kappa}{\partial s}\int_0^s \kappa U\, ds'. \tag{3}$$

Further details are provided in Appendix. Plugging relation (1) into (3) yields the governing equation for the geometrical evolution of the leading edge as a function of the graded actin density.

C. Actin density

The actin network is a dynamic structure that constantly remodels. This remodeling is executed by numerous proteins that are engaged in a range of biochemical events and cascades. For example, transmembrane proteins, such as G protein coupled receptors, recruit actin-associated proteins (AAPs) and activate other signaling molecules near the membrane. The Arp2/3 complex is an AAP responsible for forming new branches from mother filaments [34]. The Arp2/3 alone is inactive; members of the Wiskott-Aldrich syndrome protein family are required for Arp2/3 activity [35]. Other AAPs mediate actin polymerization, capping, bundling, and more. Here we adopt a simplified view of these processes by considering a coarse grained description of the main three mechanisms underlying the remodeling of the actin network [4], namely, polymerization, branching, and capping. We assume that these processes take place mainly along the leading edge, that the events of branching and capping are proportional to the local actin density through rate constants c_b and c_c, respectively, and that capped filaments lag behind the leading edge. These assumptions lead to the following equation for the local actin density along the leading edge:

$$\frac{\partial \rho(s,t)}{\partial t} + \frac{\partial}{\partial s}(\rho V) = C\rho. \tag{4}$$

Here the left-hand side is an advection equation representing the conservation of ρ for $C = 0$. The right-hand side adds a source term where $C = c_b - c_c$ is the effective branching-capping rate constant. The actin network is organized in a dendritic array. The 70° branches mediated by the Arp2/3 complex, in conjunction with evolution and selection, lead to a locally symmetric distribution of filaments orientation around the normal with significant peeks at ±35° [35]. Consequently, the actin network effectively propagates in the direction normal to the leading edge [36]. This means that the growing actin network slides laterally along the leading edge, as illustrated in Fig. 4. This is accounted for in (4) by the lateral velocity $V = (\partial S/\partial t)|_\sigma$, which can be expressed in terms of the leading edge curvature [37,38], i.e.,

$$V = \int_0^s \kappa U\, ds'. \tag{5}$$

See Appendix A for further details.

III. RESULTS

Equations (3) and (4) formulate a set of nonlinear integro-partial-differential equations for the evolution of the leading edge geometry κ and for the actin density ρ. These equations are coupled through the protrusion velocity $U(\rho)$ and the lateral velocity $V(\kappa)$. This two-way coupling between the equations forms the closed loop shown in Fig. 2. Next we calculate steady-state solutions of this system.

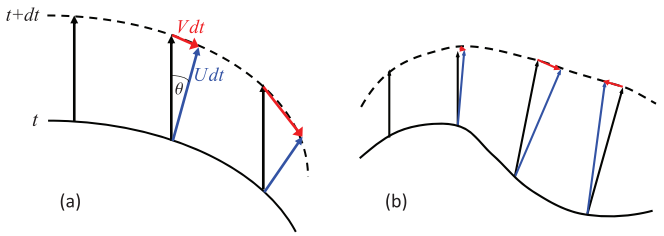

FIG. 4. (Color online) Schematic illustration of the leading edge geometry for two different times separated by dt (exaggerated). Blue, red, and dark arrows represent the normal velocity U, the lateral velocity V, and the velocity at constant s, $\partial\vec{x}/\partial t$. At steady state the black arrows are parallel and indicate the direction of propagation. This is not the case in general (see the inset). For clarity, only part of the leading edge is shown.

A. Steady-state configurations

In their pioneering work, Lee *et al.* [36] performed careful experiments that indicated that the persistent gliding motion of fish epidermal keratocytes is achieved by a graded protrusion velocity of the actin network in the direction normal to the leading edge. In addition they have shown that this graded radial extension (GRE) behavior results in a normal velocity that satisfies the relation $U = U_0 \cos\theta$, where U_0 is the cell crawling speed and θ is the angle between the crawling direction and the normal (see Fig. 4). This intriguing behavior is indeed reflected by our model since the shape equation (3) is identically satisfied by the aforementioned velocity field of the GRE behavior. In addition, it is easy to show that the lateral velocity (5) simplifies to $V = U_0 \sin\theta$ in this case. Setting $s = 0$ at the center of the lamellipodium leading edge and using the symmetry there, we calculate the steady-state solutions of (3) and (4). These are illustrated in Fig. 5. Note that the only free parameter in these equations is C, which we estimate as 7.6 ms^{-1} by fitting to the quantitative measurements of [4].

Once the steady-state configurations are calculated, it is possible to proceed along the lines of the experimental investigation of Keren *et al.* [4], i.e., study relations between some key migration features. These include the aspect ratio,

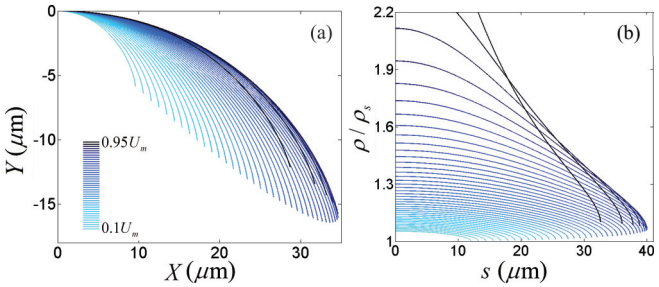

FIG. 5. (Color online) Steady-state configurations: (a) shape of the leading edge and (b) distribution of actin density along the leading edge. Crawling velocity is indicated by the color of the curve, where slower (faster) crawling velocities are lighter (darker). Due to symmetry, only the right half of the leading edge is shown.

actin ratio, front radius, speed, and area. The aspect ratio measures the ratio between the width and the length of the lamellipodia, which in terms of our model parameters equals $|x(L)/y(L)|$. The actin ratio describes the ratio between the actin concentration at the center of the leading edge and the end of the leading edge, i.e., $\rho(0)/\rho(L)$. The front radius is the radius of curvature at the center of the leading edge, which is simply $1/\kappa(0)$. The crawling speed is U_0. Finally, the area describes the area occupied by the whole cell. Since we have only investigated the lamellipodia leading edge our model cannot provide this information. In order to connect this feature to our model, we assume that the cell area is proportional to the area enclosed by the lamellipodia, which is $\int_0^L [y - y(L)] \cos\theta \, ds$. Following [4], we calculate how each of these features varies between stable steady-state configurations and find that all aforementioned features are positively correlated (see Appendix C for further details). This is in complete agreement with the experimental observations of [4].

B. Stability

We now turn to study the stability of these steady-state configurations. We call a steady-state configuration stable if it is not sensitive to small perturbations. Accordingly, we call a steady-state configuration unstable if it is possible to introduce a small perturbation such that the system will not return to the original steady state. Unfortunately, analytical linear stability analysis is not possible in this case. The reason is the coupling between the two state functions (κ and ρ) through nonlocal (integral) terms. It is possible to prove, analytically, that each of these state functions is independently stable with respect to any steady-state solution. In other words, if shape is prescribed (enforced), steady-state solutions of ρ are stable. Also, if ρ is prescribed (enforced), steady-state solutions of κ are stable. These findings have no guarantee for stability of the full (coupled) problem. Indeed, we prove by numerical analysis that some steady-state solutions of the coupled problem are unstable.

The stability of the steady-state configurations is studied numerically by simulating the dynamics of the system, using (3) and (4), after introducing a wide range of small perturbations to the steady-state configuration (see Appendix B for further details). We find that there exists a critical migration velocity above which the persistent gliding motion is unstable. In other words, it is possible to distinguish between stable and unstable steady states by their crawling velocity. Specifically, steady-state configurations with $U_0 < 0.84U_m$ are stable, while fast configurations with $U_0 > 0.84U_m$ are unstable.

Finally, we note that our simulations impose a constant value of ρ at the end of the leading edge, in accordance with experimental observations [3,4,6]. The biological meaning of this boundary condition is that at the rear sides of the leading edge, where large adhesions are located, the cell maintains a constant density of the actin network. The exact mechanism responsible for this is still unknown [4] and it is evident that the actin density at the end of the leading edge is not exactly constant, but subjected to disturbances. In order to understand the consequences of such disturbances, we study the dynamic response of steady-state configurations subjected to random

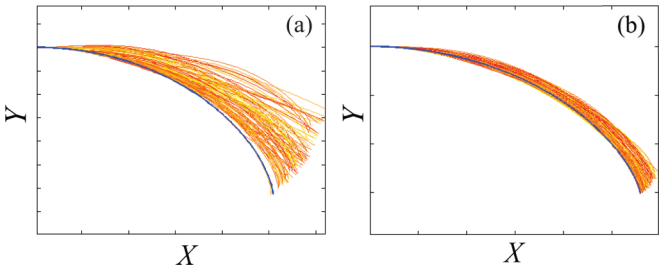

FIG. 6. (Color online) Comparison between the dynamic response (leading edge geometry at different times) of two stable steady-state configurations subjected to random fluctuations in the actin density at the end of the leading edge: (a) $U_0 = 0.2U_m$ and (b) $U_0 = 0.6U_m$. The maximum magnitude of density fluctuations is $\rho/\rho_s = 0.2$, with a correlation length of 10 s.

fluctuations in the boundary condition of ρ. Our numerical simulations show that, in slower cells, the fluctuations in ρ at the end of the lamellipodium lead to significant variations of the curvature, considerable front roughness, and large fluctuations in shape, as illustrated in Fig. 6. Moreover, these disturbances in actin density at the ends introduce what appears like traveling waves in the leading edge shape. These waves initiate at the end of the leading edge and gradually die out while advancing towards the center of the leading edge (see Fig. 7).

IV. DISCUSSION

The stable steady-state configurations obtained by our theoretical model (see Fig. 5) suggest that the crawling speed, front radius, lamellipodium length, aspect ratio of the leading edge, and actin center-to-side ratio are all positively correlated. This is in agreement with quantitative measurements of

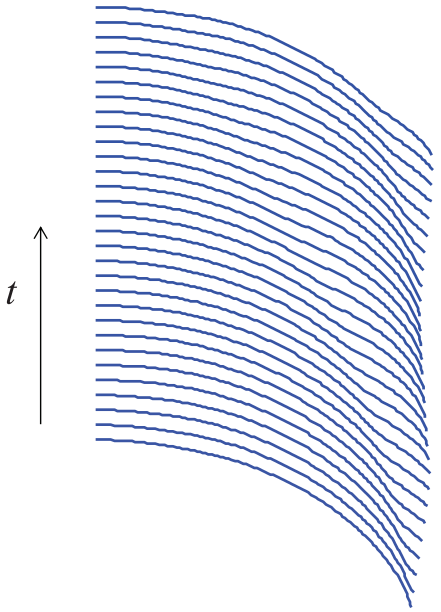

FIG. 7. (Color online) Geometry of the leading edge (only the right half is shown) at different times when subjected to random fluctuations in the actin density at the end of the leading edge: $U_0 = 0.2U_m$, with a simulation length of 40 s.

migration and morphological features in a large number of live fish keratocyte cells [4]. We note that the large dispersion in aspect ratio as a function of migration velocity observed in experiments is a consequence of the significant biological variability between cells. This is in accordance with our model predictions (e.g., by changing branching and capping rates associated with proteins concentration) and with the results of [23]. Still, experiments indicate that the migration features of an individual cell (or cell fragment) are altered by changing the substrate properties, as discussed next. These experiments show that there is a direct and monotonic relation between the cells aspect ratio and crawling velocity, as long as the cell maintains a persistent (stable) gliding motion. We also note that once the motion of the cell becomes unstable with nonpersistent shape, the aforementioned correlations do not necessarily hold.

Our model does not include adhesion explicitly, i.e., there is no parameter in the model that represents adhesion. Still, the model accounts for adhesion indirectly, as illustrated in Fig. 2, through membrane tension. Membrane tension arises mainly from the coordination between adhesion to the substrate and the forces generated by the motility machinery pushing the membrane from within the cell. Thus, generally speaking, higher adhesion leads to an increase in membrane tension [31,32,39]. This approach puts aside the details of the adhesion process. In contrast, it significantly simplifies the model and enables important insights regarding the effects of membrane tension on the lamellipodia dynamics. These effects can be qualitatively compared with experiments that study how substrate adhesion influences lamellipodia dynamics. In terms of our model parameters, membrane tension (or alternatively adhesion) increases the stall density ρ_s. This means that the nondimensional density ρ/ρ_s at the rear end of the lamellipodium decreases, resulting in a different steady-state configuration. From Fig. 5 it is evident that membrane tension (through ρ/ρ_s at the rear end) has a monotone effect on the migration velocity associated with the steady-state configuration, where lower tension results in a higher steady-state velocity. Consequently, membrane tension has a biphasic effect on the lamellipodium length and the aspect ratio; these increase between low and intermediate membrane tension and decrease between intermediate and high membrane tension. These results agree well with experimental observations [5]. Further, our analysis indicates that configurations associated with low adhesion strength (i.e., low membrane tension) are unstable. This feature is indeed observed in experiments [5]. We note that the current model does not account for the existence of retrograde flow of the actin network. Thus our calculated velocity is not the actual crawling velocity, but the actin polymerization rate. Still, experimental data indicate that the retrograde flow is not significant when crawling on surfaces with high or intermediate adhesion strength [5]. This may not be the case on surfaces with low adhesion strength. Thus our model provides a very good platform for understanding the large-scale dynamics of lamellipodia moving on substrates with intermediate-to-high adhesion strength. Importantly, even on low adhesion substrates where the competency of our model to predict the actual migration speed is questionable, it provides a very good approximation for the shape of the leading edge and for the distribution of actin density along the leading edge. Finally, in accordance with experimental observations, our model predicts high front roughness and traveling waves in the leading edge curvature in slow crawling cells (i.e., with high adhesion strength) due to high sensitivity to disturbances in the boundary conditions.

In summary, we developed a simple physical model that captures the essence of lamellipodia dynamics and explains the observed spectrum of epidermal fish keratocyte behavior. Therefore, we learn that most morphological features and migration characteristics observed in experiments are a direct consequence of the closed feedback loop between shape and actin density. Without closing this loop, steady-state configurations would not be stable and the persistent gliding motion crucial for the function of keratocyte cells could not be achieved. We also find that the maximum speed of such persistent gliding motion is limited by stability of this feedback loop. We note that the current model is missing some important ingredients such as direct account for adhesion and for myosin-mediated contraction, graded distribution of proteins along the leading edge, and the existence of a retrograde flow of the actin network. These are expected to refine the results, but will not alter the main insights provided here.

ACKNOWLEDGMENTS

We thank an anonymous referee for insightful comment on the derivation of the geometrical evolution equation (3). This derivation appears in Appendix A. This work was supported by the Israel Science Foundation, Grant No. ISF 1500/10.

APPENDIX A: LATERAL VELOCITY

The shape equation (3) and the lateral velocity (5), which appears in Eq. (4), are central equations to the model. In particular, V describes the rate at which the actin network moves laterally (slides) along the leading edge. We note that Eq. (3) and expression (5) have already been obtained elsewhere, e.g., [37,38]. We derive these equations here for completeness, though by a different approach.

We begin by writing

$$\frac{\partial \kappa}{\partial t} = -\hat{n} \cdot \frac{\partial^2}{\partial s^2}\left(\left.\frac{\partial \vec{x}}{\partial t}\right|_s\right), \tag{A1}$$

which immediately follows from (2). In the orthogonal gauge, where $\frac{\partial \vec{x}}{\partial t} = U\hat{n}$, one can show that

$$\left.\frac{\partial \vec{x}}{\partial t}\right|_s = \left.\frac{\partial \vec{x}}{\partial t}\right|_\sigma + \left.\frac{\partial \vec{x}}{\partial \sigma}\frac{\partial \sigma}{\partial t}\right|_s = U\hat{n} - \left.\frac{\partial s}{\partial t}\right|_\sigma \hat{t}. \tag{A2}$$

Above, relations $\frac{\partial \sigma}{\partial t}|_s = -\frac{1}{\sqrt{g}}\frac{\partial s}{\partial t}|_\sigma$ and (2) have been used for the second equality. Using the definition of the lateral velocity $V = \frac{\partial s}{\partial t}|_\sigma$, we find by plugging (A2) into (A1) that

$$\frac{\partial \kappa}{\partial t} = -V\frac{\partial k}{\partial s} + \left(\kappa^2 - \frac{\partial^2}{\partial s^2}\right)U - 2\kappa\frac{\partial V}{\partial s}. \tag{A3}$$

Next, by direct differentiation of $s(\sigma,t) = \int_0^\sigma \sqrt{g(\sigma',t)}d\sigma'$ with respect to time and using some algebraic manipulations

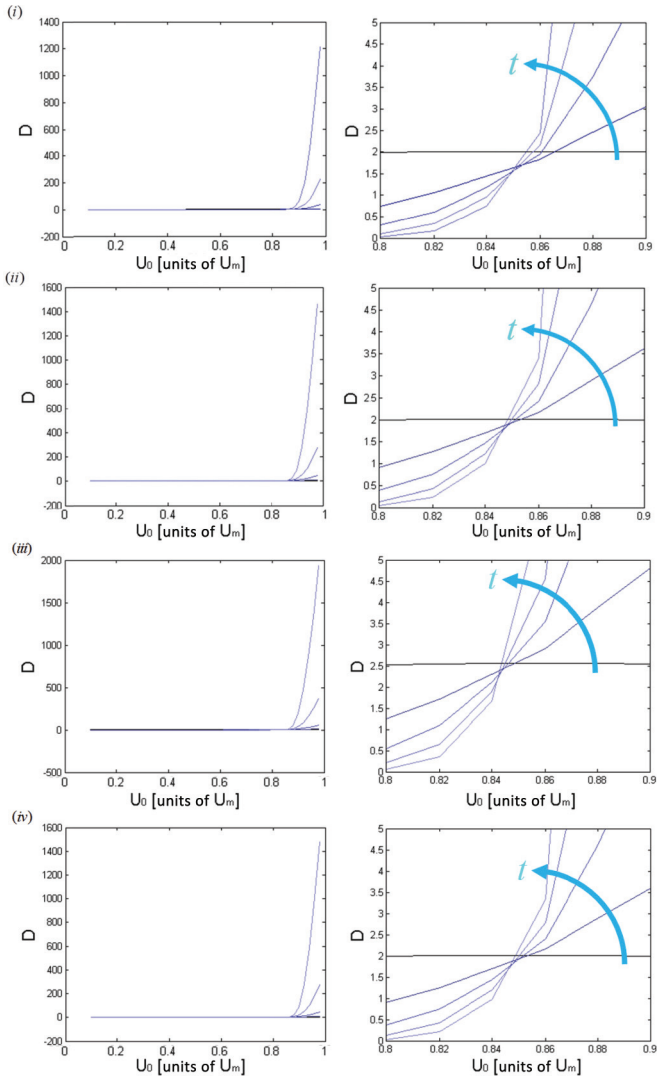

FIG. 8. (Color online) Deviation $D(t) = \int_0^L |\rho - \rho^*| ds$ from the steady-state solution ρ^* as a function of U_0 for perturbations types (i)–(iv) in Eq. (B1). The graphs on the right are identical to those on the left, but focused on the region $0.8U_m \leqslant U_0 \leqslant 0.9U_m$. In each plot, the different lines correspond to a different time $t = 0,250,500,750,1000$ s.

we obtain

$$V = \int_0^s U\kappa \, ds'. \tag{A4}$$

Finally, inserting (A4) into (A3), we conclude with the shape equation (3).

Next, we formally derive the left-hand side of Eq. (4). In particular we formulate the conservation law for ρ assuming $C = 0$. Recalling that the actin network effectively grows in the normal direction, we write

$$\frac{d}{dt}\left(\int_{s(\sigma_1,t)}^{s(\sigma_2,t)} \rho \, ds\right) = 0, \tag{A5}$$

where σ_1 and σ_2 are arbitrary. Thus we have that

$$\int_{s(\sigma_1,t)}^{s(\sigma_2,t)} \frac{\partial \rho}{\partial t} ds + \left(\frac{\partial s(\sigma,t)}{\partial t}\rho\right)\Big|_{s(\sigma_1,t)}^{s(\sigma_2,t)} = 0 \tag{A6}$$

and therefore

$$\int_{s(\sigma_1,t)}^{s(\sigma_2,t)} \left(\frac{\partial \rho}{\partial t} + \frac{\partial(\rho V)}{\partial s}\right) ds = 0, \tag{A7}$$

where we have used the definition of the lateral velocity, i.e., $V = \frac{\partial s(\sigma,t)}{\partial t}$. Since the domain of integration is arbitrary, we conclude with Eq. (4).

APPENDIX B: NUMERICAL STABILITY

We investigated the stability of steady-state configurations numerically. To this end, we introduced a small perturbation to the steady-state configuration and simulated the dynamics of the system using Eqs. (3) and (4). This procedure enabled us to identify unstable configurations. Also, by examining a wide range of perturbations, we were able to provide strong evidence for stability. Therefore, we have examined a wide range of perturbations in shape and in actin density, which were introduced to various steady-state configurations. We refer to a steady-state configuration as stable if it is stable with respect to all perturbations we have examined. Below we detail only the perturbations we used in a systematic analysis involving the entire range of steady-state configurations, which was used in order to identify the critical velocity separating between stable and unstable regions:

$$\delta\rho = 0.1\left(1 - \frac{s}{L}\right), \quad \delta\theta = 0.01\frac{s}{L} \quad \text{[perturbation (i)]};$$

$$\delta\rho = 0.1\left(1 - \frac{s}{L}\right), \quad \delta\theta = -0.01\frac{s}{L} \quad \text{[perturbation (ii)]};$$

$$\delta\rho = 0.1\cos\left(\frac{1}{2}\frac{\pi s}{L}\right), \quad \delta\theta = -0.01\sin\left(\frac{1}{2}\frac{\pi s}{L}\right) \quad \text{[perturbation (iii)]};$$

$$\delta\rho = 0.1\cos^2\left(\frac{1}{2}\frac{\pi s}{L}\right), \quad \delta\theta = -0.01\sin^2\left(\frac{1}{2}\frac{\pi s}{L}\right) \quad \text{[perturbation (iv)]};$$

$$\delta\rho = -0.1\left(1 - \frac{s}{L}\right)^{1/2}, \quad \delta\theta = 0.1\left(\frac{s}{L}\right)^{1/2} \quad \text{[perturbation (v)]};$$

$$\delta\rho = -0.1\cos\left(\frac{1}{2}\frac{\pi s}{L}\right), \quad \delta\theta = 0.1\sin\left(\frac{1}{2}\frac{\pi s}{L}\right) \quad \text{[perturbation (vi)]};$$

$$\delta\rho = -0.1\sin\left(\frac{5}{2}\frac{\pi s}{L}\right), \quad \delta\theta = 0.1\cos\left(\frac{5}{2}\frac{\pi s}{L}\right) \quad \text{[perturbation (vii)]};$$
$$\delta\rho = -0.1\left(1-\frac{s}{L}\right), \quad \delta\theta = 0.1\left(\frac{s}{L}\right) \quad \text{[perturbation (viii)]};$$
$$\delta\rho = 0.1\left(1-\frac{s}{L}\right), \quad \delta\theta = 0.1\frac{s}{L} \quad \text{[perturbation (ix)]}. \tag{B1}$$

We emphasize that in addition to (B1) we have examined a wide range of perturbations, including random perturbations in ρ and θ. Importantly, all these simulations support the findings of the systematic analysis performed with (B1). The systematic analysis with perturbations (B1) indicates that steady-state configurations associated with $U_0 < 0.84U_m$ are stable, while fast configurations with $U_0 > 0.84U_m$ are unstable. This is illustrated in Fig. 8, which presents the deviation from the steady-state solution $D(t) = \int_0^L |\rho - \rho^*| ds$ for perturbations (i)–(iv) in (B1), where ρ^* is the steady-state actin density. Perturbations (v)–(ix) yield similar results (not shown). It is seen that D is close to zero for steady-state configurations associated with $U_0 < 0.84U_m$. In addition, D decreases with time in this region. This means that the perturbations decrease to zero and therefore these configurations are stable. In contrast, the values of D are large and increasing with time for steady-state configurations associated with $U_0 > 0.84U_m$. Therefore, these steady-state configurations are not stable. We therefore conclude that $U_0 \simeq 0.84U_m$ is a critical velocity that separates between stable and unstable steady-state configurations.

APPENDIX C: RELATIONS BETWEEN KEY MIGRATION FEATURES

Following [4], we calculate how each of key migration features varies between stable steady-state configurations and present graphs that describe the relations between each pair in Fig. 9. All graphs show a positive slope, indicating a positive correlation between each pair's features. This is in complete agreement with the experimental observations of [4].

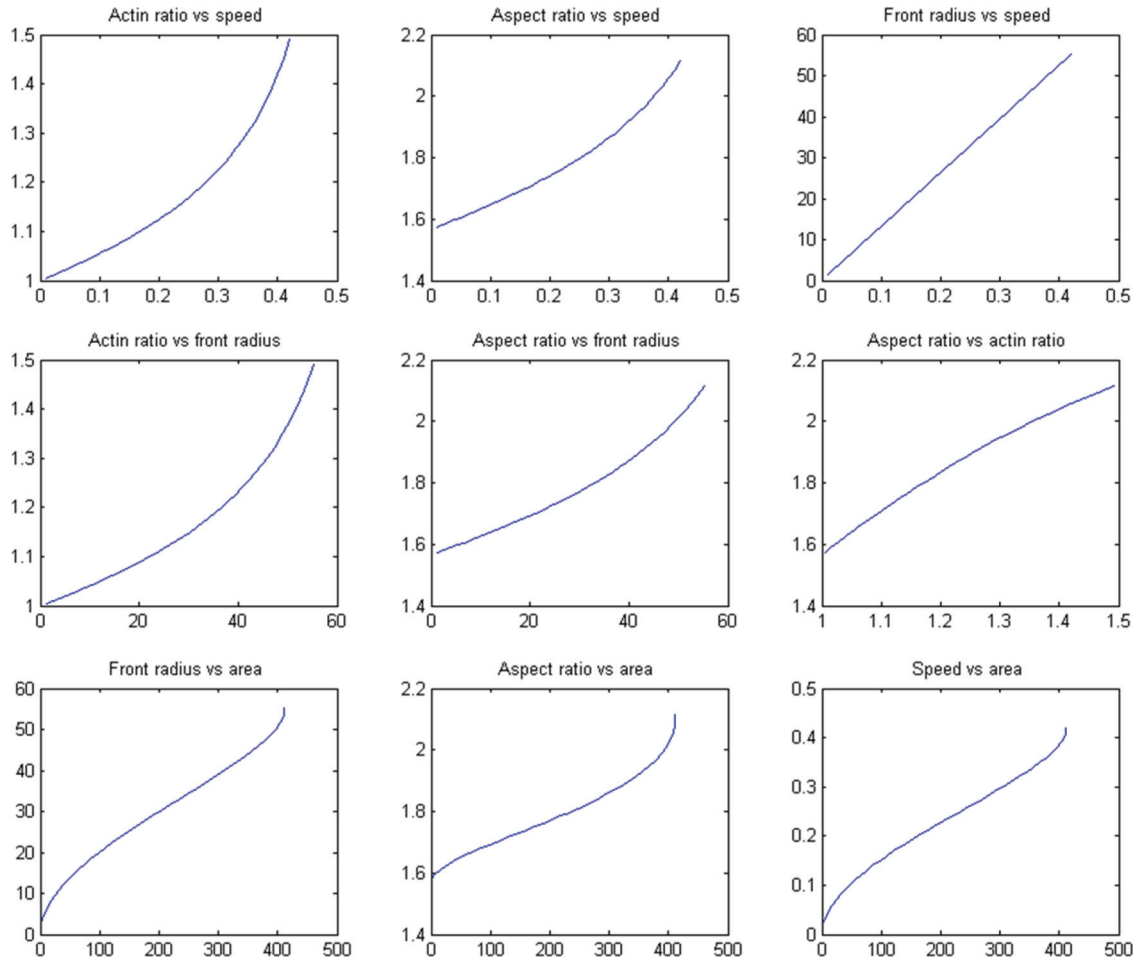

FIG. 9. (Color online) Relation between pairs of motility features of stable steady-state configurations. Front radius, area, and speed are measured in μm, μm^2, and μm s^{-1}, respectively. Aspect ratio and actin ratio are nondimensional quantities.

[1] B. Alberts, *Essential Cell Biology* (Garland Science, New York, 2004), Vol. 1.
[2] K. Anderson, Y.-L. Wang, and J. Small, J. Cell Biol. **134**, 1209 (1996).
[3] K. Keren, Eur. Biophys. J. **40**, 1013 (2011).
[4] K. Keren, Z. Pincus, G. M. Allen, E. L. Barnhart, G. Marriott, A. Mogilner, and J. A. Theriot, Nature (London) **453**, 475 (2008).
[5] E. L. Barnhart, K.-C. Lee, K. Keren, A. Mogilner, and J. A. Theriot, PLoS Biol **9**, e1001059 (2011).
[6] C. I. Lacayo, Z. Pincus, M. M. VanDuijn, C. A. Wilson, D. A. Fletcher, F. B. Gertler, A. Mogilner, and J. A. Theriot, PLoS Biol. **5**, e233 (2007).
[7] N. Ofer, A. Mogilner, and K. Keren, Proc. Natl. Acad. Sci. USA **108**, 20394 (2011).
[8] J. Fort and T. Pujol, Rep. Prog. Phys. **71**, 086001 (2008).
[9] J. Fort and V. Méndez, Phys. Rev. Lett. **82**, 867 (1999).
[10] J. F. Douglas, K. Efimenko, D. A. Fischer, F. R. Phelan, and J. Genzer, Proc. Natl. Acad. Sci. USA **104**, 10324 (2007).
[11] V. Ferreiro, J. F. Douglas, J. Warren, and A. Karim, Phys. Rev. E **65**, 051606 (2002).
[12] J. Fort and V. Méndez, Phys. Rev. Lett. **89**, 178101 (2002).
[13] A. L. Garner, Y. Y. Lau, T. L. Jackson, M. D. Uhler, D. W. Jordan, and R. M. Gilgenbach, J. Appl. Phys. **98**, 124701 (2005).
[14] J. Merikoski, J. Maunuksela, M. Myllys, J. Timonen, and M. J. Alava, Phys. Rev. Lett. **90**, 024501 (2003).
[15] B. Rosenstein, B. Y. Shapiro, and I. Shapiro, Europhys. Lett. **70**, 506 (2005).
[16] V. S. Zykov and K. Showalter, Phys. Rev. Lett. **94**, 068302 (2005).
[17] P. DiMilla, J. Stone, J. Quinn, S. Albelda, and D. Lauffenburger, J. Cell Biol. **122**, 729 (1993).
[18] A. Huttenlocher, M. Ginsberg, and A. Horwitz, J. Cell Biol. **134**, 1551 (1996).
[19] S. Palecek, J. Loftust, M. Ginsberg, D. Lauffenburger, and A. Horwitz, Nature (London) **385**, 537 (1997).
[20] W. R. Holmes and L. Edelstein-Keshet, PLoS Comput. Biol. **8**, e1002793 (2012).
[21] D. Shao, H. Levine, and W.-J. Rappel, Proc. Natl. Acad. Sci. USA **109**, 6851 (2012).
[22] D. Shao, W.-J. Rappel, and H. Levine, Phys. Rev. Lett. **105**, 108104 (2010).
[23] F. Ziebert, S. Swaminathan, and I. S. Aranson, J. R. Soc. Interface **9**, 1084 (2012).
[24] U. Seifert, Adv. Phys. **46**, 13 (1997).
[25] S. Givli, H. Giang, and K. Bhattacharya, SIAM J. Appl. Math. **72**, 489 (2012).
[26] T. Schaus and G. Borisy, Biophys. J. **95**, 1393 (2008).
[27] A. Mogilner, Curr. Op. Cell Biol. **18**, 32 (2006).
[28] M. Prass, K. Jacobson, A. Mogilner, and M. Radmacher, J. Cell Biol. **174**, 767 (2006).
[29] K.-C. Lee and A. Liu, Biophys. J. **97**, 1295 (2009).
[30] S. Parekh, O. Chaudhuri, J. Theriot, and D. Fletcher, Nat. Cell Biol. **7**, 1219 (2005).
[31] A. Hategan, R. Law, S. Kahn, and D. Discher, Biophys. J. **85**, 2746 (2003).
[32] A. Mogilner and K. Keren, Curr. Biol. **19**, R762 (2009).
[33] R. C. Brower, D. A. Kessler, J. Koplik, and H. Levine, Phys. Rev. A **29**, 1335 (1984).
[34] R. Mullins, J. Heuser, and T. Pollard, Proc. Natl. Acad. Sci. USA **95**, 6181 (1998).
[35] E. Atilgan, D. Wirtz, and S. Sun, Biophys. J. **89**, 3589 (2005).
[36] J. Lee, A. Ishihara, J. Theriot, and K. Jacobson, Nature (London) **362**, 167 (1993).
[37] R. E. Goldstein and D. M. Petrich, Phys. Rev. Lett. **67**, 3203 (1991).
[38] K. Nakayama, H. Segur, and M. Wadati, Phys. Rev. Lett. **69**, 2603 (1992).
[39] A. D. Lieber, S. Yehudai-Resheff, E. L. Barnhart, J. A. Theriot, and K. Keren, Curr. Biol. **23**, 1409 (2013).